AJNR

Temporal Resolution of Dynamic Angiography Using Flat Panel Volume CT: In Vivo Evaluation of Time-Dependent Vascular Pathologies

R. Gupta, A. Mehndiratta, A.P. Mitha, M. Grasruck, C. Leidecker, C. Ogilvy and T.J. Brady

R. Gupta
A. Mehndiratta
A.P. Mitha
M. Grasruck
C. Leidecker
C. Ogilvy
T.J. Brady

Temporal Resolution of Dynamic Angiography Using Flat Panel Volume CT: In Vivo Evaluation of Time-Dependent Vascular Pathologies

BACKGROUND AND PURPOSE: Recently introduced fpVCT scanners can capture volumetric (4D) time-varying projections enabling whole-organ dynamic CTA imaging. The main objective of this study was to assess the temporal resolution of dynamic CTA in discriminating various phases of rapid and slow time-dependent neurovascular pathologies in animal models.

MATERIALS AND METHODS: Animal models were created to assess phasic blood flow, subclavian steal phenomena, saccular aneurysms, and neuroperfusion under protocols approved by the SRAC. Animals with progressively increasing heart rate—*Macaca sylvanus* (~100 bpm), *Oryctolagus cuniculus* (NZW rabbit) (~150 bpm), *Rattus norvegicus* (~300 bpm), *Mus musculus* (~500 bpm)—were imaged to challenge the temporal resolution of the system. FpVCT, a research prototype with a 25 × 25 × 18 cm coverage, was used for dynamic imaging with the gantry rotation time varying from 3 to 5 seconds. Volumetric datasets with 50% temporal overlap were reconstructed; 4D datasets were analyzed by using the Leonardo workstation.

RESULTS: Dynamic imaging by using fpVCT was capable of demonstrating the following phenomena: 1) subclavian steal in rabbits ($\Delta T \cong 3$–4 seconds); 2) arterial, parenchymal, and venous phases of blood flow in mice ($\Delta T \cong 2$ seconds), rabbits ($\Delta T \cong 3$–4 seconds), and *Macaca sylvanus* ($\Delta T \cong 3$–4 seconds); 3) sequential enhancement of the right and left side of the heart in *Macaca sylvanus* and white rabbits ($\Delta T \cong 2$ seconds); and 4) different times of the peak opacification of cervical and intracranial arteries, venous sinuses, and the jugular veins in these animals (smallest, $\Delta T \cong 1.5$–2 seconds). The perfusion imaging in all animals tested was limited due to the fast transit time through the brain and the low contrast resolution of fpVCT.

CONCLUSIONS: Dynamic imaging by using fpVCT can distinguish temporal processes separated by >1.5 seconds. Neurovascular pathologies with a time constant >1.5 seconds can be evaluated noninvasively by using fpVCT.

ABBREVIATIONS: ACA = anterior cerebral artery; AVF = arteriovenous fistula; AVM = arteriovenous malformation; bpm = beats per minute; CBF = cerebral blood flow; CBV = cerebral blood volume; CE = contrast enhanced; CTA = CT angiography; DSA = digital subtraction angiography; ECA = external carotid artery; fps = frames per second; fpVCT = flat panel volume CT; ICA = internal carotid artery; IVC = inferior vena cava; MDCT = multidetector row CT; MIP = maximum intensity projection; MTT = mean transit time; NZW = New Zealand white; RCCA = right common carotid artery; SRAC = Subcommittee on Research Animal Care; SSS = subclavian steal syndrome

In many institutions including ours, MDCT has replaced DSA for routine vascular imaging. A CTA by using intravenous contrast injection provides quantitative high-resolution 3D images by using a minimally invasive technique. CTA, however, is a static snapshot of the vascular anatomy and pathology under consideration. Its inability to reveal dynamic features of any time-varying phenomena and its vulnerability to metal artifacts demands the intermittent need for DSA for flow-related information and for follow-up after surgical clipping or coil treatment.

The advent of dynamic CT holds the promise of obviating DSA for diagnostic purposes by enabling noninvasive visualization of time-varying phenomena. As such, MDCT scanners

are increasingly being used for visualizing dynamic processes such as cardiac function, neuroperfusion, time-resolved angiography, and the dynamics of a first-pass contrast bolus in a variety of vascular pathologies.[1] The newer generation of CT scanners supports wider z-coverage and faster gantry-rotation time. In addition, modern scanners allow back-and-forth helical motion of the patient table in a volume of interest to enable 4D imaging. These so-called "shuttle modes" allow a trade-off between volumetric coverage and temporal resolution.[2] Because the temporal resolution of these 4D techniques is limited—typically 0.5–5 seconds between successive datasets compared with 30 frames/second for DSA—it is essential to define their boundaries in elucidating various time-dependent phenomena.

Depending on the process being observed, if the temporal resolution is short enough and the imaging is conducted for an appropriate length of time, the evolution of a contrast bolus can be followed through the arteries, visceral parenchyma, and veins. With such a dataset, a perfusion study of these tissues can be performed, making it possible to combine both angiography and perfusion in 1 dynamic imaging process.

Table 1: Variation in heart rates of animals used for validating the temporal resolution of fpVCT in vascular pathology models		
Animal	Heart Rate (bpm)	No.
Macaca sylvanus	100	2
NZW rabbit	150	17
Rattus norvegicus	300–400	3
Mus musculus	500–600	13

Table 2: Different animals used for each dynamic study protocol and time-dependent vascular models created in each animal			
Dynamic Study	Animal	No.	Model
Phases of blood flow	*Macaca sylvanus*	2	Healthy control
	NZW rabbit	10	Healthy control
	Mus musculus	10	Healthy control
Aneurysm filling	NZW rabbit	10	Modified elastase aneurysm model
Tumor blood flow	NZW rabbit	4	VX2 tumor model
Time-dependent pathologies	NZW rabbit	1	Subclavian steal model
Neuroperfusion (CBV, CBF, MTT)	NZW rabbit	2	Stroke model
	Rattus norvegicus	3	ECA ICA filament
	Mus musculus	3	ECA ICA filament

This article evaluates the dynamic imaging capabilities of a prototype fpVCT scanner using an area detector mounted on a conventional CT gantry with slip rings. Such a configuration has the ability to perform conebeam CT, allowing volumetric whole-organ coverage. The gantry can rotate continuously while acquiring projection data, giving it the added capability of 4D-CT scanning. This article assesses the potential of this new technique in a sequence of progressively more demanding dynamic imaging situations in animal models of vascular anatomy and pathology.

Animal models were created to assess phasic blood flow, subclavian steal phenomena, flow in and around a saccular aneurysm, and neuroperfusion. Animals with progressively increasing heart rate were imaged to challenge the temporal resolution of the imaging system.

The ability to distinguish different phases of blood flow was evaluated in *Macaca sylvanus*, *Oryctolagus cuniculus* (NZW rabbit), *Rattus norvegicus,* and *Mus musculus* (approximate heart rates of 100 bpm, 150 bpm, 300–400 bpm, and 500–600 bpm, respectively) (Table 1). The adequacy of the temporal resolution of 4D-CTA for discriminating the various phases of blood flow—that is, sequential enhancement of the vessels—was assessed. Because these processes represent a wide spectrum of time differences in peak opacification, it is to be expected that they will reveal the limit of the temporal resolution of the fpVCT scanner rotating at 3 seconds, the fastest rotation time available on our prototype scanner.

Materials and Methods

fpVCT Scanner and Dynamic Imaging

An fpVCT scanner is a variant of the conventional MDCT scanner in which the individual rows of detectors have been replaced by a 2D digital flat panel detector. In the prototype system, the digital flat panel detector (PaxScan 4030CB; Varian Medical Systems, Palo Alto, California) was integrated with a Sensation-64 (Siemens Medical Solutions, Forchheim, Germany) CT gantry.

The flat panel detector consists of a matrix of 2×1.5 K detector elements, each measuring 194 μm^2,[3] having an active area of 40×30 cm. Therefore, the in-plane FOV is approximately 25 cm, with volumetric coverage in the z-direction up to 18 cm.[4,5] This is large enough to scan an entire human head, heart, or liver in 1 rotation. The rotation time of the gantry can be varied from 2 to 20 seconds. The native spatial resolution of the flat panel at the isocenter is 150 μm^3.

From the projection data acquired during $\geq$1 rotation, individual CT sections, with an isometric voxel size of approximately 150 μm^3, are reconstructed by using a modified algorithm of Feldkamp et al.[6] To take into account even the slightest deviations of the gantry position during a rotation, we measured the angular position of each projection by using a slip ring while the projection data were being acquired. These precisely measured nonequidistant angular positions were then used by the reconstruction algorithm for back-projection.

The details of the reconstruction algorithm are discussed in Grasruck et al,[7] Gupta et al,[8] and Grasruck et al.[9]

The wide-area detector used by the fpVCT prototype enables one to scan from a fixed angular position with a high image frame rate and to scan continuously while the gantry is rotating. This flexibility gives rise to a number of scanning modes including ultra-high resolution, fluoroscopy, and dynamic scanning. Ultra-high resolution and fluoroscopy have been described previously.[1,5] The dynamic CT mode, the focus of this article, is described below.

FpVCT has the ability to monitor a temporally evolving process by acquiring temporally varying projection data. In the current prototype, a volume of interest measuring 25×25 cm in-plane and 18 cm in the z-direction, can be observed for a total of 80 seconds; the gantry rotation time can be varied from 2 to 20 seconds.

The projection data provide a temporal log of the viewing volume, which is converted into multiple 3D volumes displaced in time. These image volumes or the 4D stack capture the temporal evolution of a process under observation.[4,7,8] To reconstruct a volumetric dataset at any time (t), one can simply use the projections from 360° centered on time t. A 4D representation of a dynamic process, by using overlapping or nonoverlapping 3D datasets, can thus be reconstructed.

The dynamic reconstruction of a 4D dataset works in 2 steps: First, all the projection data are preprocessed to apply offset correction, gain calibration, defective pixel correction, lag correction, and beam-hardening correction. The convolution filter is then applied with a preselected convolution kernel. In a second step, several 3D image sets are back-projected at each user-defined set of time points to generate a set of 3D volumes.[7-9] Each 3D volume represents a time point, and loading all the volumes in sequential order will generate a 4D dataset.

The temporal resolution of such a dataset will be equal to the rotation time of the gantry. In general, a higher rotation speed improves the temporal resolution at the expense of image noise and spatial resolution. Multiple phases in a time-evolving process could be visualized in 4D by using appropriate visualization software.[4,7-9] The time increment between successive 3D volumes can be arbitrarily chosen.

Subclavian Steal Model

Under a protocol approved by the SRAC at Massachusetts General Hospital (protocol 2005N000217), a subclavian steal model was surgically created in a rabbit (Table 2). Before all procedures, anesthesia was induced by using a single administration of acepromazine (1 mg/kg), ketamine (50 mg/kg), and xylazine (5 mg/kg), and animals were allowed to breathe spontaneously. Following induction, fur over the ventral neck was shaved and the skin was prepared by using a

betadine solution. A 5- to 8-cm midline neck incision was made rostrally from the level of the sternum. The right sternocleidomastoid and sternohyoid muscles were retracted laterally, with dissection revealing the underlying right brachiocephalic and subclavian arteries.

A permanent 1-0 silk ligature was then placed around the right subclavian artery proximal to the origin of the vertebral artery. The wound was then closed by using running subcuticular 3–0 Vicryl suture (polyglactin 910; Ethicon, Cornelia, Georgia), and 3 weeks were allowed for hemodynamic stabilization. After this period, the rabbit was again anesthetized and scanned with an fpVCT scanner to visualize the flow pattern and time gap between the opacification of the 2 subclavian arteries.

Intracranial Saccular Aneurysm Model

A model of an intracranial aneurysm was created in 10 NZW rabbits (Table 2) weighing 3–4 kg (Charles River Laboratories, Germantown, Maryland) (Massachusetts General Hospital SRAC protocol 2005N000217). Anesthesia was induced by using the same regimen described previously, and the surgical exposure of the RCCA was achieved similarly. Dissecting the tissues overlying the RCCA exposed the origin of the vessel from the brachiocephalic bifurcation. A 3–0 silk ligature was used to occlude the RCCA distally, approximately 3 cm from its origin, and a temporary aneurysm clip was placed at the origin of the vessel. A 24-ga angiocatheter was then inserted just proximal to the site of ligation, and 100 U of porcine pancreatic elastase (Worthington Biochemical, Lakewood, New Jersey) was infused into the lumen of the isolated vessel segment and allowed to incubate for 20 minutes. A 3–0 silk ligature was then tied just proximal to the angiocatheter entry site; later the angiocatheter and temporary aneurysm clip were both removed. The skin was subsequently closed by using a running subcuticular 3–0 Vicryl suture. Following aneurysm creation, the animals were allowed to recover for 3 weeks, during which hemodynamic factors combined with the weakened vessel wall resulted in formation of a saccular aneurysm.[1,10,11]

Neurovascular Perfusion

An ischemia model was created in the 2 NZW rabbits (Table 2) by ligating the RCCA to compare CBV, CBF, and MTT changes in both hemispheres. Anesthesia induction, dissection, and the carotid ligation procedure have been described above. The animals were given a sufficient recovery time of 3 weeks for hemodynamic stability before the scan was obtained. *Rattus norvegicus* (*n* = 3) and *Mus musculus* (*n* = 3) (Table 2) were also used to create an ischemia model by advancing a filament from the ECA to the ICA to completely occlude the ICA. Brain scans were obtained on these animals, and perfusion maps were derived by using the Patlak model.

Phasic Blood Flow

Two Macaques (*Macaca sylvanus*) (Table 2) were anesthetized with the same protocol as described earlier for rabbits, and contrast-enhanced dynamic brain scans were obtained to demonstrate the sequential blood flow from the arterial to the parenchymal to the venous phase. Ten NZW rabbits (Table 2) were scanned under the same protocol to study the temporal evolution of cardiac and pulmonary circulation. Ten healthy white albino mice (*Mus musculus*) (Table 2) were also scanned to study the pulmonary circulation time by injecting the contrast in the tail vein and observing the enhancement of the thoracic aorta.

Table 3: CT acquisition settings used for static and dynamic scanning protocol for each animal

Animal	Tube Voltage (kV[peak])	Tube Current (mAs)	Gantry Rotation Time (sec)	Total CE Scanning Time (sec)
Macaca sylvanus	100	50	5	70–80
NZW rabbit	120	50	5	45
Rattus norvegicus	100	30	5	60
Mus musculus	100	30	5	55–60

FpVCT Scanning, Postprocessing, and Evaluation

Scanning. All animals were scanned under the anesthesia regimen described earlier. After positioning the animal in a holder and fixation of all extremities, we obtained an orientation noncontrast scan at tube voltage and tube currents described in Table 3 with a standardized gantry rotation of 19 seconds and a projection acquisition time of 20 seconds. This scan was obtained for orientation and for acquiring an initial noncontrast image dataset.

The noncontrast scan was followed by contrast-enhanced dynamic CT of the region of interest. These regions were imaged continuously for 45–60 seconds with a rotation time of 5 seconds, at gantry parameters mentioned in Table 3. Contrast agent (iopamidol 370, Isovue 370; Bracco Diagnostics, Princeton, New Jersey), at a dose of 3 mL/kg of body weight, was used for dynamic scanning in all the animal models. Dynamic scans for Macaques and NZW rabbits were obtained with a contrast flow rate of 3 mL/s through femoral intravenous access by using an automated injector (Mark IV; Medrad, Indianola, Pennsylvania). Dynamic scans for *Rattus norvegicus* and *Mus musculus* were obtained with a contrast flow rate of 0.1–0.3 mL/s through tail vein access by using the same automated injector. The injector delay time was set at 5 seconds. The injector and the projection image acquisition were started simultaneously. Because of the 5-second delay, the projection images from the first rotation were without contrast. The projections from subsequent rotations of the gantry documented the evolution of the contrast bolus in the region of interest.

Postprocessing and Evaluation. The reconstructed datasets were supplemented with a DICOM header that allowed importation into a standard image-processing workstation. The datasets were postprocessed with InSpace software (Leonardo workstation; Siemens, Erlangen, Germany). The postprocessing consisted of reformatting oblique planes through each 3D CT stack, segmentation, and volume rendering. For dynamic visualization of the untreated, clipped, or coiled aneurysms, multiple 3D datasets were displayed by using the 4D capabilities of the workstation.

Axial and oblique reformatted sections from fpVCT, 4D images from dynamic fpVCT, and projection images were independently evaluated by 2 readers (R.G. and A.M.).

Results

Phasic Blood Flow

Temporal resolution of 4D-CTA was sufficient to discriminate the early arterial, late arterial, parenchymal, and venous equilibration phases for most of the animal models. 4D datasets clearly distinguished the arterial from the venous phase of circulation in time and space. The 4D angiograms have a spatial resolution of approximately 200 μm^3. This enabled visualization of even the distal arterial branches supplying the brain parenchyma. For example, in the scan of a Macaque, the
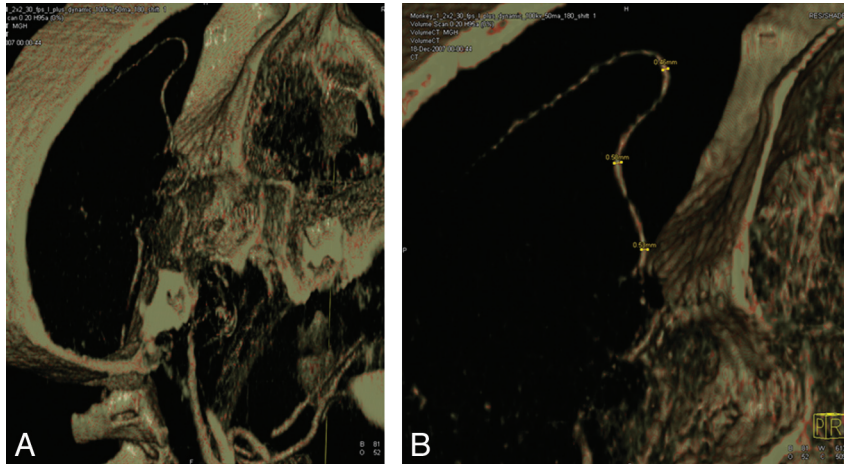
Fig 1. Zoomed-in view of the ACA (of *Macaca sylvanus*) at the peak of arterial opacification. Nearly the entire course of the ACA, with a diameter <200 μm in the distal portions, is visualized because of the excellent resolution afforded by the digital flat panel technology.
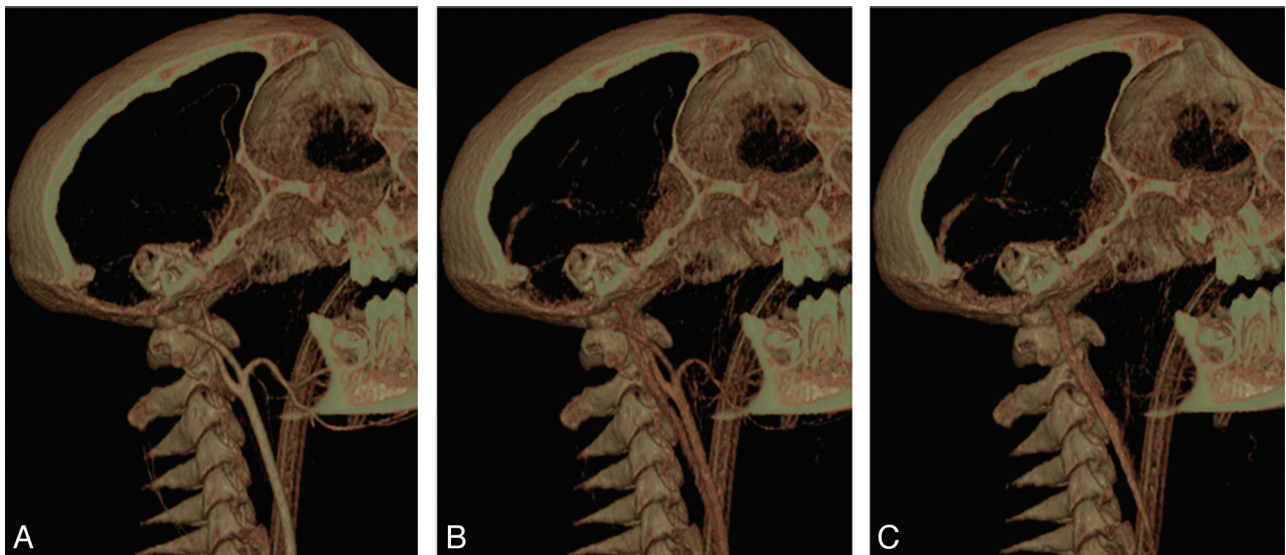

Fig 2. Time-resolved MIP images through a sagittal slab of the brain parenchyma of a *Macaca sylvanus* showing arterial, parenchymal, and venous phases of circulation in this animal with a heart rate of approximately 150 bps.

course of the ACA (measuring 0.46 mm proximally) is very well visualized (Fig 1). Dynamic imaging (Fig 2) showed the sequential filling of the common carotid artery, ICA, and ACA, followed by slow filling of venous sinuses draining in the neck veins. The projection data acquired at 30 fps revealed that the time difference between the peak enhancement of the common carotid artery and the internal jugular vein was on the order of 15 seconds (Table 4). The reconstructed images with a temporal resolution of 2.5 seconds (approximately half the gantry rotation time) were able to separate this 15-second interval into the arterial, parenchymal, and venous phases (Table 4).

Phasic blood flow through the various thoracic and abdominal structures in the *Mus musculus* after a tail vein injection was also elaborated with respect to sequential opacification of the tail vein, IVC, heart, aorta, and kidney perfusion. Projection data (Table 4) confirmed the time point of sequential opacification.

An even more challenging situation was presented by the temporal sequence of neurovascular opacification in *Rattus*

norvegicus. Despite the short transit time through the brain, sequential opacification of the arterial, parenchymal, and venous phases of neurovascular circulation could be delineated by time-resolved 4D angiography (Fig 3).

Subclavian Steal Model

The dynamic CT images of the subclavian steal model in the NZW rabbit demonstrated delayed enhancement of the right subclavian artery compared with the left side. On the raw projection images, the peak opacification times were 5 and 7.5 seconds in the left and right subclavian arteries, respectively (Table 4). This time difference was perceptible in the 4D image sets. The early frames showed enhancement of the aortic arch, brachiocephalic artery, the left common carotid artery, and the left subclavian artery (Fig 4), with a lack of contrast in the right subclavian artery because of the surgically created proximal occlusion. In subsequent frames, progressive enhancement of the right subclavian via the right vertebral artery can be appreciated.

Table 4: Results of each dynamic process and animal model comparing the time measured using 30-fps projection acquisition and visualization in dynamic 4D datasets after image reconstruction

Dynamic Process Being Monitored	Anatomic Location and Flow Pattern	Actual Time from Projection Data, 30 fps (sec)	Animal Model	Visualization in Dynamic 4D Datasets (gantry rotation time = 5 sec)
Cerebral circulation	Common carotid artery to internal jugular vein	15	*Macaca sylvanus*	Yes
Cerebral circulation	Common carotid artery to internal jugular vein	12.3–13.3	NZW rabbit	Yes
SSS model	Anomalous circulation	5–7.5	NZW rabbit	Yes
Pulmonary circulation	IVC to aorta,	5.3	NZW rabbit	Yes
	right heart to left heart,	3	NZW rabbit	Yes
	tail vein to heart,	2–3	*Mus musculus*	Yes
	heart to abdominal aorta,	2–3	*Mus musculus*	Yes
	IVC to right heart	2.3	NZW rabbit	Yes
Pulmonary circulation	Right heart to left heart,	<2	*Mus musculus*	No
	left heart to common carotid artery,	1.33	NZW rabbit	No
	tail vein to IVC,	<1	*Mus musculus*	No
	IVC to right heart,	<1	*Mus musculus*	No
	left heart chamber to aorta	<1	*Mus musculus*	No
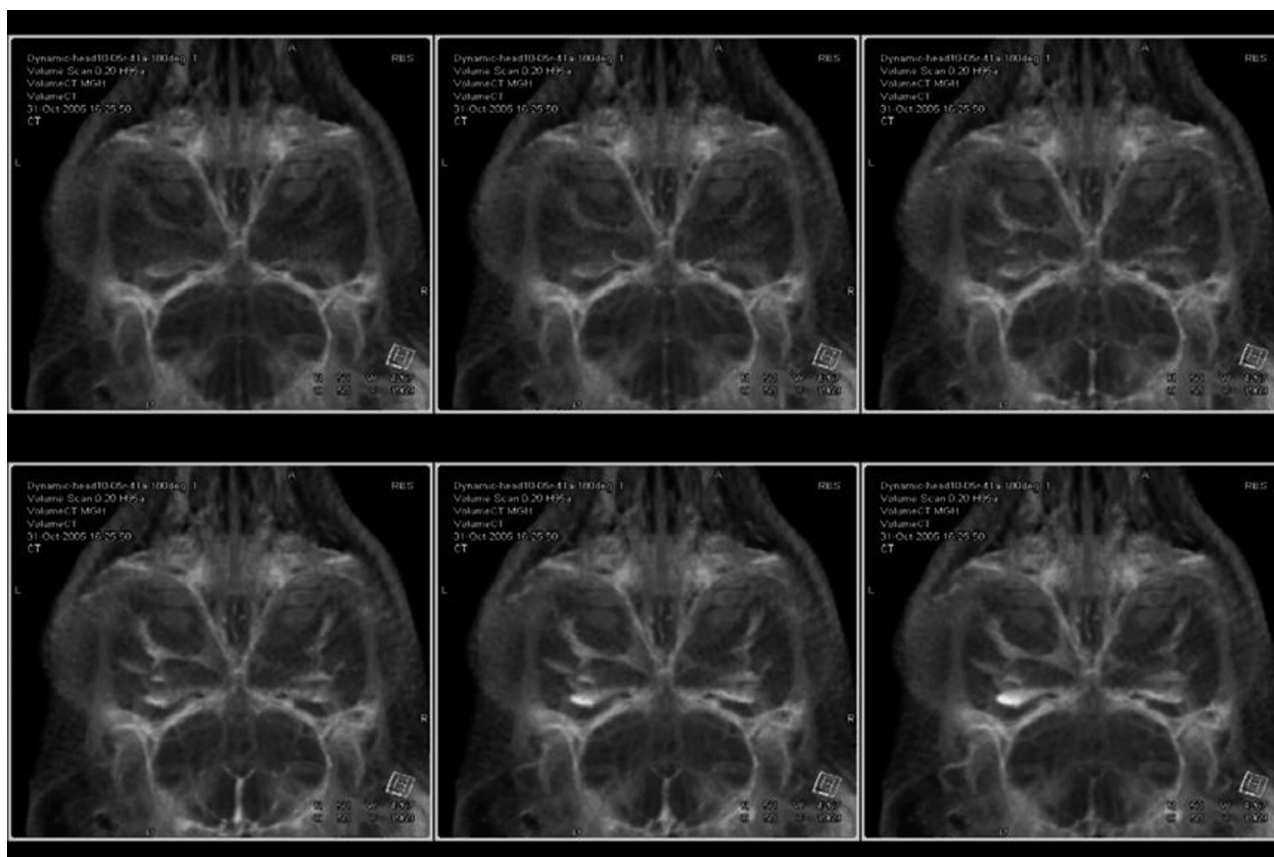
Fig 3. Six sequential frames showing opacification of the arteries, parenchyma, and the veins of the brain in a *Rattus norvegicus* model. In the parenchymal phase, the contrast enhancement of the brain is only minimally above the baseline value because of the contrast resolution of the scanner.

Brain Perfusion and Ischemia Model

The temporal resolution of fpVCT was sufficient to analyze the parenchymal phase of contrast enhancement to derive perfusion maps for the rabbit brain (in a stroke model) by using the Patlak model. While the main phases of perfusion could be visualized, the results were equivocal in visualizing small MTT differences (<1–1.5 seconds) created by proximal carotid occlusion. Figure 5 shows the time-attenuation curves in a feeding cerebral artery and a draining vein in the brain study. This time-attenuation curve indicates that though the rotation time was 5 seconds (temporal resolution of ~2.5 seconds), the method of temporally overlapping reconstructions used was able to resolve the short cerebral transit time of approximately 3 seconds. The image quality of the deriver perfusion maps, however, is suboptimal, primarily because of the low contrast resolution of the scanner.

An ischemia model was prepared in *Rattus norvegicus*, by percutaneously inserting a filament in the left ECA, advancing it proximally to the carotid bifurcation, engaging the origin of the left ICA, and advancing it further to occlude the left ICA.
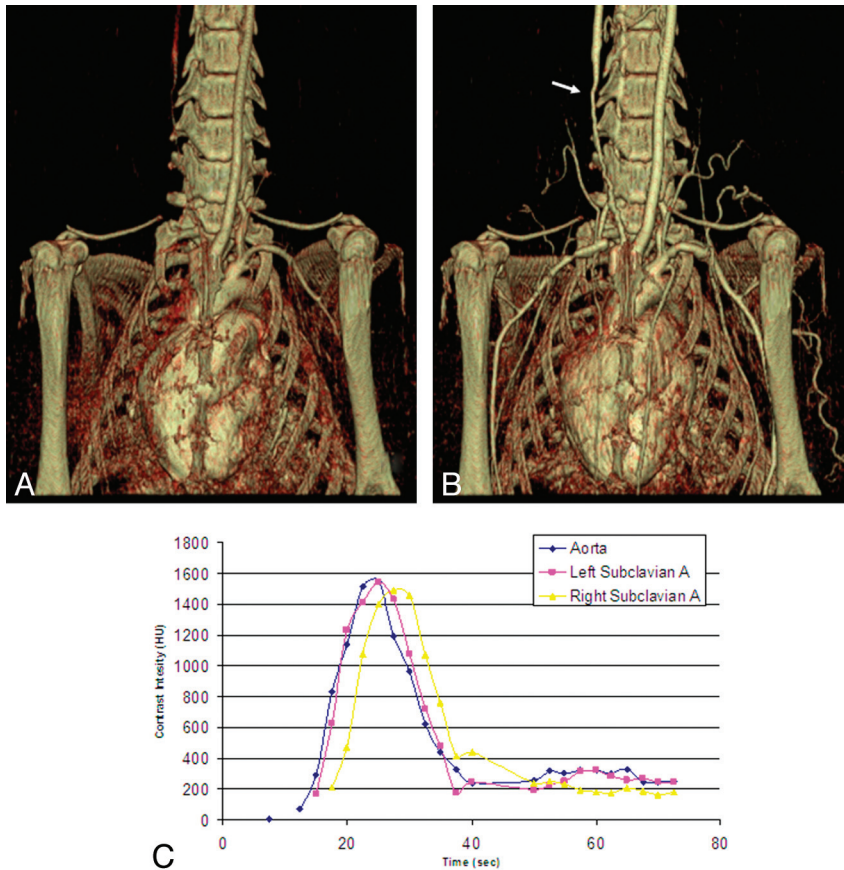
Fig 4. Demonstration of subclavian steal phenomenon by using dynamic CTA in a NZW rabbit model. *A*, An early arterial phase MIP image shows opacification of the left subclavian, left vertebral, and left common carotid arteries. *B*, A late arterial phase image shows opacification of the right subclavian artery via retrograde flow (reverse flow) from the right vertebral artery. Note the chemical vasculitis induced in the RCCA from an intra-arterial injection of elastase, which was used to demonstrate endothelial injury in this artery before scanning. *C*, Contrast intensity (HU) vs time curve showing the temporal delay in peak enhancement of right subclavian artery (*yellow*) with respect to aorta (*blue*) and left subclavian artery (*pink*).

Sample time-attenuation curves for the left and right cerebral hemispheres are shown in Fig 6. The perfusion maps derived from this model were also unable to demonstrate the transit time difference between the left and right side of the brain due to limitations of the temporal and contrast resolution of the fpVCT scanner.

Rabbit Aneurysm Model
In the rabbit aneurysm model, aneurysm pulsatility could not be visualized secondary to motion artifacts from cardiac and pulmonary movements and less than adequate temporal resolution. Although one could appreciate a change in the appearance of the aneurysm sac and neck from 1 phase to the next, the change in appearance was deemed unreliable because the images were not acquired with cardiac or respiratory gating. The change in appearance was likely related to progressive change in the density of contrast in the aneurysm sac rather than true pulsation. The 4D images were also not informative about turbulent flow of contrast inside the aneurysm sac due to insufficient temporal resolution. On the other hand, the blood flow pattern around the aneurysm, in terms of distinguishing the arteries and veins, was readily discernable.

Discussion
In current clinical practice, 2 imaging modalities play a central role because of their complementary nature: Angiography is

used to visualize temporally varying processes while CT is used for static anatomy. Dynamic CT imaging by using a digital flat-panel detector can potentially satisfy demands of both of these 2 very different modalities, making a combined noninvasive 4D examination feasible.

This study was designed to evaluate the feasibility of 4D-CTA by using fpVCT. The dynamic imaging capabilities of fpVCT were used to assess, in vivo, clinically relevant flow-related hemodynamic processes such as phasic blood flow, steal phenomena, intracranial aneurysms, and neuron perfusion. We conducted experiments on 4 different animals, with progressively increasing heart rates (and therefore, tissue transit times) to elucidate the limits of the temporal resolution offered by such a scanner. For time differences involving the major blood vessels, the peak opacification time from the raw projection images, acquired 33.33 ms apart, was taken as the criterion standard. No criterion standard was available for the brain perfusion part of this study. Therefore, all conclusions regarding the feasibility of perfusion imaging by using fpVCT are based on qualitative evaluation of the data.

At the temporal resolution offered by the scanner (-2.5 seconds), one could appreciate the dynamics of the first-pass bolus transit in and around the aneurysm. We were able to demonstrate important time-dependent phenomena such as subclavian steal and different phases of blood flow. Perfusion imaging, however, required substantial in-plane spatial
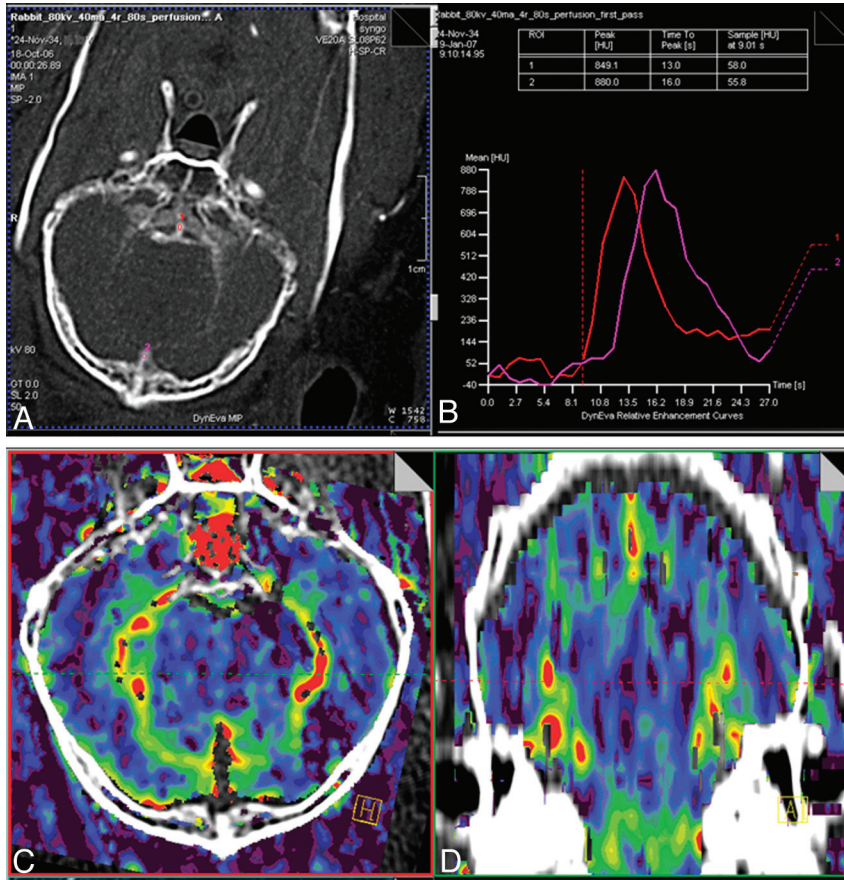
Fig 5. *A*, An axial section through a single phase of a 4D time-resolved image stack used for estimating brain perfusion. The arterial and venous inputs used for computation are marked. *B*, Arterial and venous time opacification curves. *C* and *D*, Axial and coronal CBV maps computed by using the Patlak model.
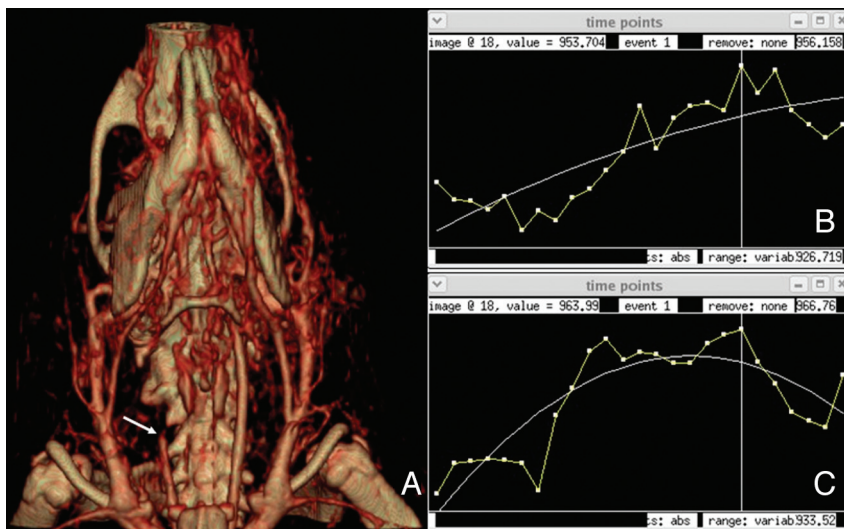

Fig 6. *A*, A frame from the arterial phase of a dynamic scan obtained on a rat with occlusion of the proximal right ICA (*arrow*). The right ICA was occluded via a filament inserted in the ECA and then advanced into the ICA. *B* and *C*, Time-attenuation curves of the brain parenchyma on the right (*B*) and left (*C*) side of the brain. The perfusion maps derived from this model were unable to demonstrate the transit time difference between the left and right side of the brain due to limitations of the temporal and contrast resolution of the fpVCT scanner.

smoothing to reduce image noise before perfusion maps could be derived from the raw data. The resolution in the z-direction was also drastically reduced by reconstruction with a section thickness of 2 mm and an increment of 1 mm. Despite considerable spatial smoothing, the contrast-to-noise ratio was limited, as evidenced by the patchy appearance of the brain pa-

renchyma. The whole-brain perfusion maps showed only gross differences in the perfusion parameters; the fine alterations in the CBV or MTT introduced by either clamping the common carotid artery or blocking the ICA with a filament could not be resolved.

The high spatial resolution offered by the fpVCT scanner

Fig 7. Image showing aneurysm creation used in NZW rabbit models: 3D reconstructions of an aneurysm by using fpVCT (left) and MDCT (right). Despite the small size of this aneurysm, the anatomy of the aneurysm sac, including a small bleb (*arrow*), can be well visualized by using fpVCT. The surface anatomy is considerably smoothed, and no bleb is identified with MDCT.

did demonstrate surface features such as nipples or projections in the aneurysm. These features are believed to carry an increased risk of rupture.[10,12] Dynamic imaging of surgically created aneurysms was unable to demonstrate the pulsation or filling pattern of blood within the aneurysm sac because of lack of cardiac and respiratory gating.

Both AVMs and AVFs of the brain are congenital tangles of abnormal vessels that demonstrate high flow. Noninvasive characterization of the flow dynamics of these lesions can be helpful in endovascular treatment planning. Dynamic angiography by using fpVCT can potentially be used for this purpose. In the past, experimental animal models of AVMs have been described for radiologic, histologic, and radiosurgical purposes. For example, porcine rete mirabile, a tangle of naturally occurring microvessels, has been used to simulate human AVMs.[13,14] In these models, increased blood flow through the retia mirabiliais is achieved by a surgical side-to-side anastomosis between the carotid artery and the ipsilateral jugular vein. Multiple carotid artery branches also need to be embolized for this model to function as an AVM. A sheep model of an AVM has also been described.[15]

All these complex models, which require considerable surgical and neurointerventional skill to create, are necessary to faithfully simulate the physiology of human AVMs for radiosurgery or interventional studies. However, to determine if human AVMs can be characterized by using noninvasive dynamic imaging, all we need is fast blood flow. Fast transit time though the brain in animals with high heart rates can offer requisite blood flow patterns to test the temporal resolution of the fpVCT system, obviating a complex surgically created AVM or AVF.

The temporal resolution of the fpVCT scanner is similar to some of the volumetric scan modes available on MDCT scanners (eg, Adaptive Spiral CT by Siemens Medical Solutions and Volume Shuttle Mode CT by GE Healthcare, Milwaukee, Wisconsin). In these modes, to increase the volumetric coverage, one can move the patient table back and forth while the images are being acquired. With the higher z-translation of the patient bed, the temporal resolution of the acquired 4D scan is lower. Our results demonstrate that the dome of temporal limitations observed by using fpVCT will also be seen in these modes.

Conclusions

Dynamic CTA by using fpVCT has sufficient temporal resolution to elucidate first-pass and recirculation dynamics of the contrast bolus to reveal pathologies such as steal phenomena and phasic blood flow. Brain perfusion, in the animal models tested, was of limited utility: While the perfusion maps could be derived, they were uninformative about induced ischemia or transit-time alterations due to limited contrast and temporal resolution of the scanner, respectively. The pulsation and filling pattern of the aneurysm sac could not be observed because of low temporal resolution.

References

1. Mitha AP, Reichardt B, Grasruck M, et al. **Dynamic imaging of a model of intracranial saccular aneurysms using ultra-high-resolution flat-panel volumetric computed tomography: laboratory investigation.** *J Neurosurg* 2009;111:947–57

2. Konstas AA, Goldmakher GV, Lee TY, et al. **Theoretic basis and technical implementations of CT perfusion in acute ischemic stroke. Part 2. Technical implementations.** *AJNR Am J Neuroradiol* 2009;30:885–92

3. Roos PG, Colbeth RE, Mollov I, et al. **Multiple-gain-ranging readout method to extend the dynamic range of amorphous silicon flat panel imagers.** *Proc SPIE* 2004;5368:139–49

4. Popescu S, Stierstorfer K, Flohr T, et al. **Design and evaluation of a prototype volume CT scanner.** *Proc SPIE* 2005;5745:600–08

5. Gupta R, Grasruck M, Suess C, et al. **Ultra-high resolution flat-panel volume CT: fundamental principles, design architecture, and system characterization.** *Eur Radiol* 2006;16:1191–205

6. Feldkamp LA, Davis LC, Kress JW. **Practical cone-beam algorithm.** *J Opt Soc Am* 1984;1:612–19

7. Grasruck M, Gupta R, Reichardt B, et al. **Combination of CT scanning and fluoroscopy imaging on a flat-panel CT scanner.** *Proc SPIE* 2006;61422J

8. Gupta R, Bartling S, Ross WR, et al. **Benefits of ultra-high spatial resolution in head CT: experimental assessment.** In: *Proceedings of the 88th Scientific Assembly and Annual Meeting of the Radiological Society of North America*, Chicago, Illinois; December 1–6, 2002

9. Grasruck M, Suess C, Stierstorfer K, et al. **Evaluation of image quality and dose on a flat-panel CT scanner.** *Proc SPIE* 2005;5745:179–88

10. Sekhar LN, Heros RC. **Origin, growth, and rupture of saccular aneurysms: a review.** *Neurosurgery* 1981;8:248–60

11. Hoh BL, Rabinov JD, Pryor JC, et al. **A modified technique for using elastase to create saccular aneurysms in animals that histologically and hemodynamically resemble aneurysms in human.** *Acta Neurochir (Wien)* 2004;146:705–11

12. Frerichs KU, Stieg PE, Friedlander RM. **Prediction of aneurysm rupture site by an angiographically identified bleb at the aneurysm neck.** *J Neurosurg* 2000;93:517

13. De Salles AA, Solberg TD, Mischel P, et al. **Arteriovenous malformation animal model for radiosurgery: the rete mirabile.** *AJNR Am J Neuroradiol* 1996;17:1451–58

14. Massoud TF, Ji C, Vinuela F, et al. **An experimental arteriovenous malformation model in swine: anatomic basis and construction technique.** *AJNR Am J Neuroradiol* 1994;15:1537–45

15. Qian Z, Climent S, Maynar M, et al. **A simplified arteriovenous malformation model in sheep: feasibility study.** *AJNR Am J Neuroradiol* 1999;20:765–70